Correspondence to:

L. H. Yeo,
li.yeo@colorado.edu

Laboratory Simulation of Solar Wind Interaction With Lunar Magnetic Anomalies

Li Hsia Yeo[1,2,3] , **Jia Han**[1,4] , **Xu Wang**[1,2,3], **Greg Werner**[2,3], **Jan Deca**[1,2,3] , **Tobin Munsat**[1,2,3] , and **Mihály Horányi**[1,2,3]

[1]Department of Physics, University of Colorado, Boulder, CO, USA, [2]Laboratory of Atmospheric and Space Physics, University of Colorado, Boulder, CO, USA, [3]Institute for Modeling Plasma, Atmospheres and Cosmic Dust, NASA/SSERVI, Boulder, CO, USA, [4]Now at Ecole Polytechnique Fédérale de Lausanne, Lausanne, Switzerland

Abstract Magnetic anomalies on the surface of the Moon interact with the solar wind plasma flow, resulting in both magnetic and electrostatic deflection/reflection of charged particles. Consequently, surface charging in these regions differs from regions without magnetic fields. Using the Colorado Solar Wind Experiment facility, this interaction is investigated with high-energy flowing plasmas (100–800 eV beam ions) that are incident upon a magnetic dipole embedded beneath an insulating surface. The dipole moment is perpendicular to the surface. The plasma potential distribution is measured above the surface using an emissive probe. In the dipole lobe regions the surface is charged to significantly higher positive potentials by the un-magnetized ion beam impinging on the surface while the electrons remain excluded by the magnetic field. At low ion beam energies the results agree with these expectations as the surface potential follows the ion beam energy. However, at high beam energies, the surface potentials in the electron-shielded lobe regions remain significantly lower than the expected magnitude. Surprisingly, electrons are detected in the shielded regions by a Langmuir probe. A test particle simulation indicates that secondary electrons induced by the high energy ion beams impinging on the surface can enter the shielded regions, thus lowering the surface potential.

1. Introduction

The Moon lacks a global magnetic field, but localized crustal magnetic anomalies are distributed across the lunar surface. The strengths of Lunar Magnetic Anomalies (LMAs) range between 0.1 and 1,000 nT, and their sizes range from less than 1 km to more than 100 km (Mitchell et al., 2008). Previous studies have explored several aspects of the interactions between the solar wind and these magnetic anomalies. For example, it has been found that the shock-like interaction of the solar wind with strong crustal magnetic fields can result in magnetic enhancements, which have been detected at the lunar limbs (Halekas et al., 2006; Lin et al., 1998; Russell & Lichtenstein, 1975). Lunar Prospector found evidence of mini-magnetospheres with a plasma density cavity detected near a strong crustal magnetic source (Halekas et al., 2008). Significant reduction of the back-scattered hydrogen flux from the lunar surface was observed by Chandrayaan-1 (Wieser et al., 2010) and Chang'E-4 (Wang et al., 2021; Xie et al., 2021) over large-scale magnetic anomalies, with high solar wind deflection efficiencies (Lue et al., 2011). Kaguya (SELENE) observed magnetic mirroring of electrons and ions (Saito et al., 2010), electrostatic solitary waves (Hashimoto et al., 2010), as well as electric fields created above the anomalies due to charge separation (Saito et al., 2012). Such electrostatic fields over small-scale anomalies have also been observed to result in the deflection of solar wind protons (Lue et al., 2011).

LMAs often coincide with lunar swirls, which are regions of significant albedo variations. However, the relationship between these two features is not yet fully understood and several models have been proposed to explain the origin of swirls (Blewett et al., 2011). One proposal is that LMAs were formed by cometary impacts that scoured the regolith surface and deposited new material in a manner that, when cooled below the Curie temperature, resulted in magnetic remnants (Pinet et al., 2000; Schultz & Srnka, 1980; Starukhina & Shkuratov, 2004). The exposed fresh material is believed to form the swirl patterns. Alternatively, a solar wind standoff model suggests that the magnetic anomalies may deflect solar wind protons away from the lunar surface, preventing maturation of the regolith by space weathering (Deca et al., 2018; Glotch et al., 2015; Hemingway et al., 2015; Hendrix et al., 2016; Hood & Schubert, 1980; Kramer, Besse, et al., 2011; Kramer, Combe, et al., 2011). A third model involving dust transport suggests that small, charged dust particles with high-albedo can be redistributed by enhanced surface electric fields as a result of the solar wind interactions with the LMAs (Garrick-Bethell
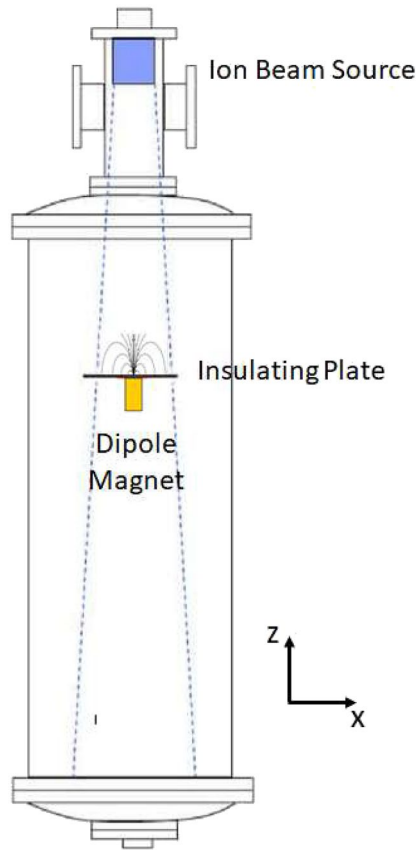
Figure 1. Schematic of the experimental setup.

et al., 2011; Hendrix et al., 2016). In this work we focused on the surface electrical environment as a result of the solar wind interaction with LMAs to help understand both the solar wind standoff and dust transport models.

Because LMAs have large variations in size and magnetic field strength, a wide range of interactions can take place between them and the solar wind. For large-scale magnetic anomalies (10 nT at 100 km altitude and >1,000 km in size), the deflection of the solar wind can be modeled with magneto-hydrodynamic (MHD) methods (Harnett & Winglee, 2000). When the solar wind dynamic pressure is balanced by the magnetic pressure, solar wind standoff occurs. However, standoff has also been observed at weak, isolated, small-scale anomalies (3 nT at 30 km altitude and <100 km in size) (Lue et al., 2011). In these examples, the solar wind electrons are magnetized with smaller gyroradii of <10 km, but the solar wind ions remain un-magnetized with gyroradii of >1,000 km. This leads to the breakdown of MHD approximations, and kinetic effects become more important (Deca et al., 2014, 2015; Usui et al., 2017; Zimmerman et al., 2015). While the magnetized electrons are deflected and/or reflected, the ions do not feel a strong magnetic force and penetrate deeper, resulting in charge separation, and the buildup of an ambipolar electric field that subsequently deflects the ions. A fraction of the un-magnetized solar wind ions may reach the surface, and in the absence of electrons, charge the surface positively. Futaana et al. (2013) observed, using the remote energetic neutral atom imaging technique, that the surface potential in the Gerasimovich magnetic anomaly is larger than +135 V. Based on conditions in this observation, Jarvinen et al. (2014) developed a hybrid simulation with a magnetic dipole setup and predicted a +300 V surface potential in the Gerasimovich anomaly region. Fatemi et al. (2015) extended this result with their hybrid simulation using the magnetic field configuration observed by Lunar Prospector and various upstream solar wind conditions.

Though the complex magnetic field configurations of LMAs and the solar wind flow are difficult to reproduce in laboratory experiments, this study focused on the understanding of the fundamental processes of the interaction of a high-energy flowing plasma with a simple magnetic dipole field. In our setup, electrons are magnetized and ions remain un-magnetized. Our previous laboratory experiments reported on charging on a surface embedded in a magnetic dipole field with non-flowing (Wang et al., 2012, 2013) and flowing (Howes et al., 2015) plasmas with ion flow energies below 55 eV. These studies showed that for a dipole moment perpendicular to the surface, the surface charges to a positive potential matching the ion flow energy in the dipole lobe regions where the incoming electrons are magnetically shielded. In this study, we present experimental results with ion flow energies up to 800 eV, close to the energy range of solar wind ions.

2. Experimental Setup and Methods

Experiments are conducted using the Colorado Solar Wind Experiment (CSWE) facility (Ulibarri et al., 2017) (Figure 1). CSWE is housed in a stainless steel, cylindrical chamber 76 cm in diameter and 182 cm in length. It uses a large cross-section Kaufman ion source with a plasma beam diameter of 12 cm, which can reach an ion flow energy of 1.2 keV and ion flow current density of 0.1 mA/cm². The chamber is typically operated at pressures of 4–6 × 10⁻⁵ Torr, low enough that ion-neutral collisions are largely suppressed. Diagnostic tools, including a Langmuir probe, an emissive probe, and an ion energy analyzer, are mounted on a motorized two-dimensional translation stage, which accurately moves the instruments both along (Z direction) and across (X direction) the plasma flow (Figure 1). The Langmuir probe is a 3 mm diameter sphere mounted on a thin insulating stand and is used to measure the electron density and temperature. Local electric poten-

Table 1
Comparison of Laboratory and Lunar Plasma Parameters

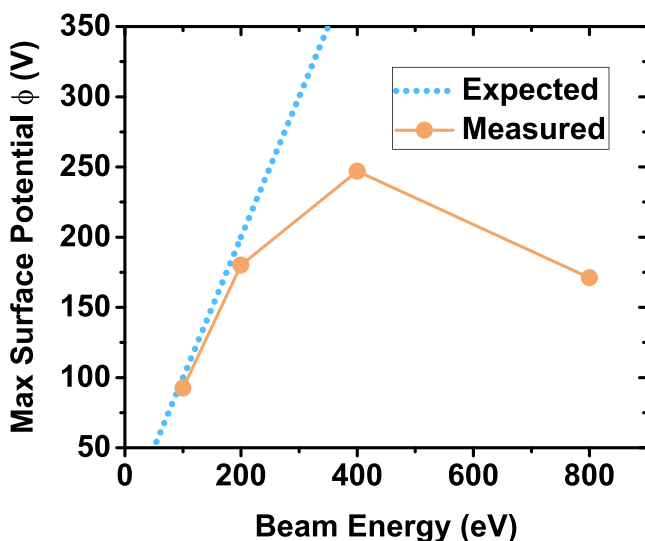|	Laboratory	Lunar
Electron gyro-ratio (r_e/L)	<<1 (10^{-4} cm/2 cm)	<<1 (0.35 km/30 km)
Electron Debye ratio (λ_e/L)	<1 (0.2 cm/2 cm)	<<1 (0.01 km/30 km)
Ion gyro-ratio (r_i/L)	>1 (15 cm/2 cm)	>1 (150 km/30 km)
Ion Debye ratio (λ_i/L)	<1 (0.9 cm/2 cm)	<<1 (0.1 km/30 km)
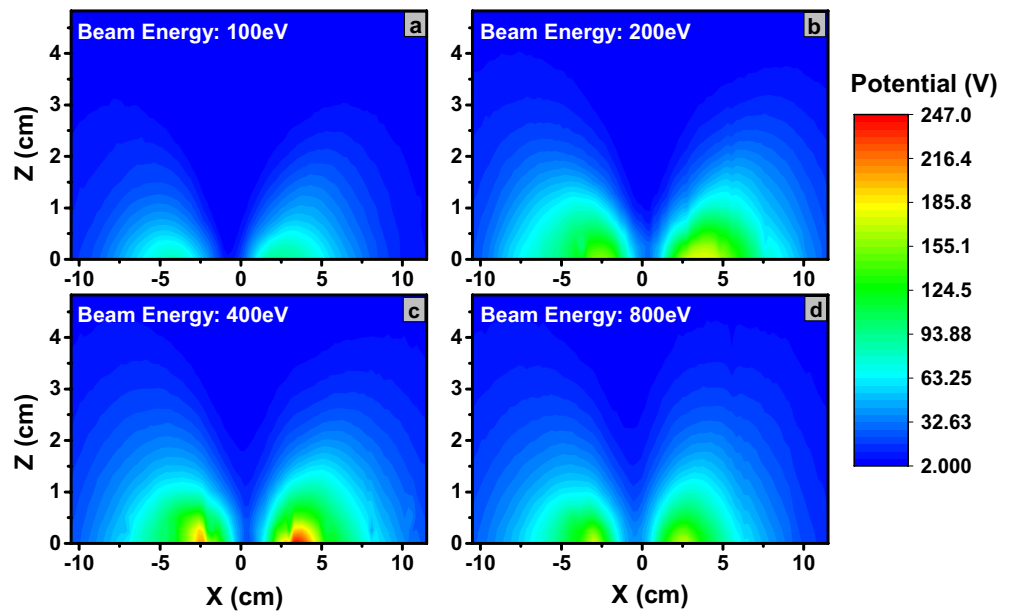
Figure 2. Potential contour plots for (a) 100 eV, (b) 200 eV, (c) 400 eV, and (d) 800 eV ion flow energies measured by an emissive probe above the surface of an insulating plate in a plane across the center of the magnetic dipole.

tials are measured with the emissive probe using the current-bias method (Diebold et al., 1988) and calibrated with the inflection point method in the limit of zero emission (Smith et al., 1979). Ion energy distributions are measured with the four-gridded energy analyzer (Böhm & Perrin, 1993).

A schematic of the experimental setup is shown in Figure 1, with plasma flowing in the negative-Z direction into the test chamber, where a 30×30 cm square insulating plate is positioned. The insulating plate is 56 cm away from the ion source that creates a flowing nitrogen plasma with ion energies in the range of 100–800 eV and ion currents in the range of 1–100 mA. The electron density is $\sim 10^7$ cm^{-3}, and the electron temperature is ~ 0.5 eV. The magnetic dipole field is created using a permanent magnet placed behind the insulating plate (Figure 1), with the dipole moment perpendicular to the plate surface, a similar arrangement used in our earlier experiments with non-flowing or with a low energy ion beam (Howes et al., 2015; Wang et al., 2012, 2013). The maximum magnetic field strength is ~ 0.14 T at the plate surface in the center of the magnet. The relevant dimensionless experimental parameters are summarized in Table 1, which are shown to be comparable to the lunar case.

3. Results

3.1. Potential Profiles With Varying Ion Energies and Currents

Figure 2 shows the potential contours measured with the emissive probe for 100, 200, 400, and 800 eV ion flow energies for the setup shown in Figure 1. In the magnetic cusp region, the quasi-neutral plasma flow reaches the surface without significant deflection, causing the surface potential to remain close to 0 V. In the lobe regions, large positive potentials are measured, in agreement with previous studies (Howes et al., 2015; Wang et al., 2012). This is because the lighter electrons are deflected by the magnetic field in these regions while the heavier ions reach the surface without much deflection by the magnetic field. The surface in this region reaches current equilibrium by developing a large enough positive potential to prevent the flow of ions to the surface. Hence, it is expected that the surface potential, measured in volts should match the ion bulk flow energy in eV to stop ions (Howes et al., 2015;
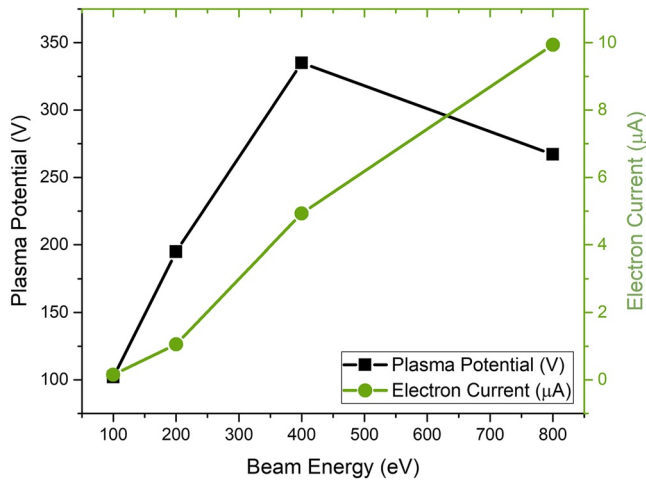

Figure 3. Maximum surface potential in the dipole lobe regions under a 5 mA ion beam with various beam energies. The expected surface potential is also plotted.
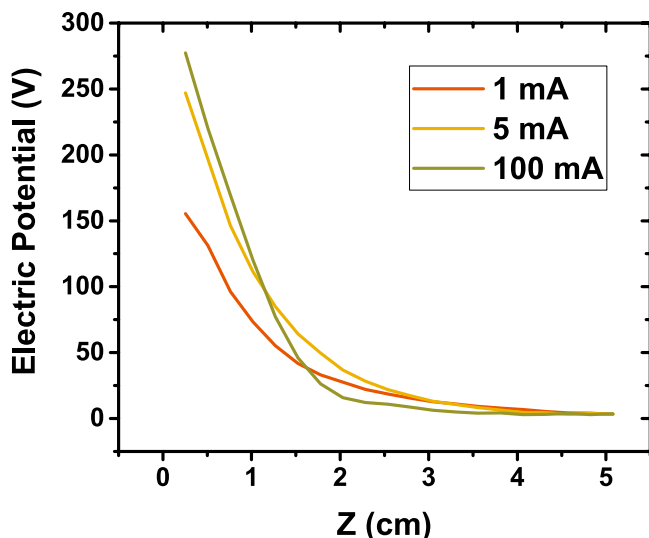
Figure 4. Plots of the local plasma potential and corresponding electron saturation current extracted from Langmuir probe I–V curves as functions of beam energy, with the probe positioned in a magnetic dipole lobe region.

Zimmerman et al., 2015). At low beam energies (100–200 eV) the measured surface potential follows this expectation. Surprisingly, at high beam energies (200–800 eV) the maximum surface potential falls significantly below its expected value (Figure 3).

### 3.2. Detection of Electrons in the Shielded Region

The lower than expected surface potentials measured at higher ion beam energies indicate the possible presence of electrons in the shielded regions, contrary to theoretical expectations (Gibson & Coppins, 2018). To examine this hypothesis, we placed a 3 mm spherical Langmuir probe just above the surface exposed to an ion beam of 400 eV and 40 mA. I–V curves were taken with the probe at various positions along the surface, perpendicular to the direction of the plasma flow. Figure 4 shows the local plasma potential and corresponding electron saturation current extracted from I to V curves taken at different beam energies in a shielded lobe region (approximately X = 35 mm, Z = 3 mm).

Figure 4 shows that local plasma potentials determined from the "knee" of the I–V curves agree with the emissive probe measurements (Figure 3). It shows substantially smaller electron currents at the local plasma potential in the lobe region at the lower beam energies of 100 and 200 eV, indicating that the electrons are mostly excluded and only the ions reach the surface. This is in agreement with the measured surface potential following the ion beam energy (Figure 3). At higher beam energies of 400 and 800 eV, the significantly increased electron currents (Figure 4) indicate the presence of electrons in the shielded lobe region, suggesting that they are responsible for lowering the surface potential.

3.3. Cause of the Electron Presence in the Shielded Regions

The question at this point is how electrons penetrate into the shielded lobe regions. Since the operating pressure of the experimental chamber is low, electron-neutral collisions are ruled out as a significant factor. In the following sections, we examine the surface electric field effect and ion-induced secondary electron emission from the surface as possible causes.

Figure 5. Measured electric potential profiles along the Z-axis in the shielded lobe region under a 400 eV ion beam with varying beam currents.

3.3.1. The Surface Electric Field Effect

Figure 2 shows measured electric potentials that reveal potential gradients both perpendicular and parallel to the surface, indicating that an outward-pointing electric field is created around each of the lobes. This electric field may be strong enough to pull electrons into the shielded regions. When the surface potential is relatively low with lower ion beam energies, the characteristic spatial scale of the electric field is small and remains enveloped within the electron-shielded region. As the ion beam energy increases, the surface is charged to a higher positive potential and the electric field extends beyond the shielded lobe regions. Electrons near the boundary of the shielded regions may now be pulled in across the magnetic field lines if the electric force is larger than the magnetic force at the boundary. This may cause the surface potential to be lower than the expected potential, and subsequently the electric field is reduced until the electron current balances the ion beam current to the surface at equilibrium.

To test this hypothesis, we measured sheath potential profiles along the Z-axis in a shielded lobe region with varying beam currents of a 400 eV ion beam (Figure 5). Figure 5 shows that the sheath potential spatial profile narrows at a higher beam current with a result of a higher surface potential. This result
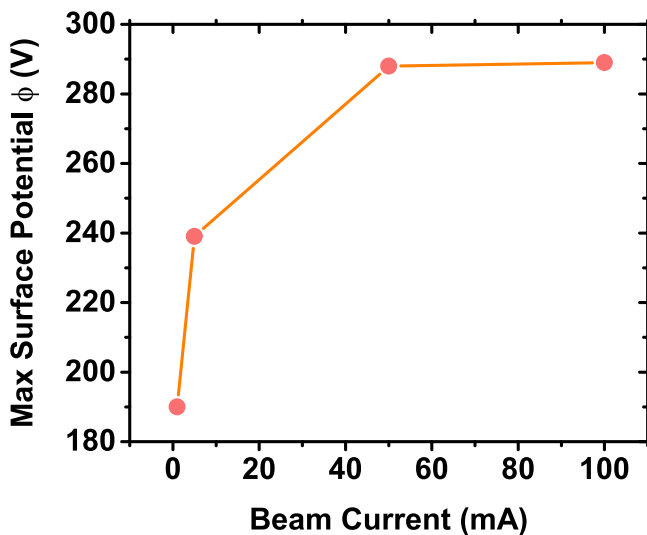
Figure 6. Maximum surface potentials measured by the emissive probe in the lobe region under a 400 eV ion beam with varying beam currents.

qualitatively agrees with our hypothesis because an increase in the beam current results in a shorter Debye length, and subsequently a narrower sheath such that fewer electrons may be pulled into the shielded region to lower the surface potential. This result also corroborates the result shown in Figure 6 demonstrating that the maximum surface potential increases with increasing beam current.
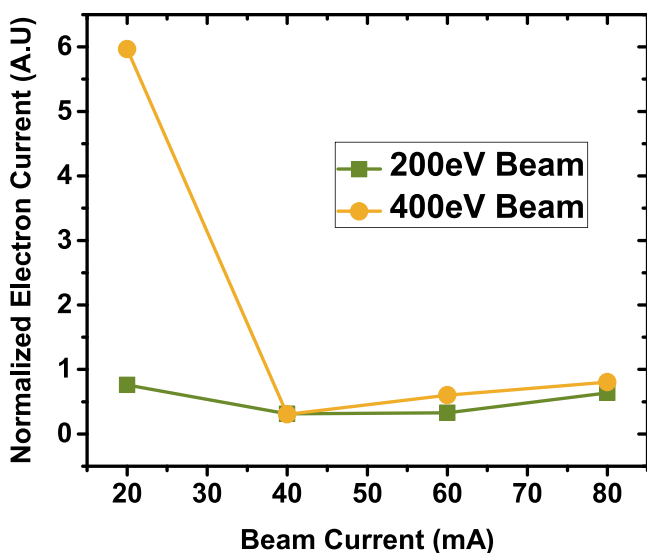
Figure 7 shows the measured electron current in the shielded lobe region as a function of the beam current. It is found that at a relatively low beam energy of 200 eV, the electron current normalized to the upstream ion beam current remains low regardless of the beam current, indicating a surface potential close to 200V. On the other hand, at a higher beam energy of 400 eV, the normalized electron current is high at the lowest beam current of 20 mA, indicating that electrons enter the shielded region and lower the surface potential. The normalized electron current drops significantly at higher beam currents, a higher surface potential is therefore expected. This result is in agreement with the trend of the maximum surface potentials with varying beam currents (Figure 6).

However, a test particle simulation using the measured magnetic and electric fields shows that the electric field force alone remains too small to pull electrons across the magnetic field lines into the shielded lobe regions (Figure 8), indicating additional processes must be involved.

3.3.2. Ion-Induced Secondary Electrons

Another possibility is that secondary electrons induced by energetic ions hitting the surface may contribute to the lowering of the surface potential by traveling into the lobe regions from the outside due to their interactions with electric and magnetic fields.

Test particle simulations were conducted in order to examine the production and subsequent trajectories of secondary electrons on the plate surface for the 100 and 800 eV beam (low and high energy, respectively) cases. The production of secondary electrons depends on the ion arrival energy at the plate surface, which in turn is dependent on initial beam energies as well as the surface electric potential. Secondary electron production rates across a range of ion energies were referenced from Knudsen and Harris (1973) and Whipple (1981). Secondary electron thermal energies were estimated to be 5 eV.

Figure 9 shows that secondary electrons are produced approximately uniformly over the entire surface area, including within the lobe ($R = 3–4$ cm) region for the 800 eV beam case because the incoming beam energy is much larger than the surface potential. On the other hand for the 100 eV beam case, secondary electrons are minimized near and within the lobe region due to significant slowing-down of the incoming beam ions. Once the secondary electrons are launched, their landing positions are determined by the magnetic and electric fields. By tracking the trajectories of these electrons, we can determine the net electron currents at different positions across the plate surface. As shown in Figure 2, the surface electric field in the lobe region points outwards, which exerts an inward force on the electrons outside and tends to pull them in. Figure 10 shows the net density of emitted and collected electrons on the surface as a function of R when 32,000 electrons were launched from the surface. It is shown that more electrons entered and were collected on the surface in the lobe region in the 800 eV beam case than in the 100 eV beam case. There are two possible reasons:

First, the lobe electric field in the 800 eV case is larger than the 100 eV case. In the 800 eV case, electrons generated between $R = 2–2.5$ cm travel an average of 0.2 mm toward the center of the lobe ($R = 3–4$ cm), but only
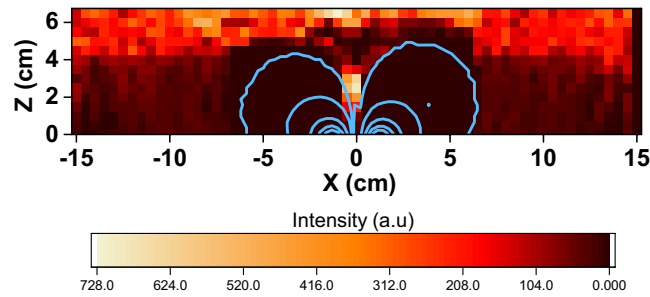

Figure 7. Ratio of the electron current to the upstream ion current as measured by a Langmuir probe in the lobe region for both low (200 eV) and high (400 eV) beam energies.

Figure 8. Density profile of electrons precipitating from above the surface by a test particle simulation with the measured magnetic and electric fields. It shows that the density of electrons is high in the cusp region, and that the electrons are shielded from entering the lobe region. Magnetic field lines are superimposed on the graph for reference.

0.04 mm for the 100 eV case. Similarly, electrons generated between $R = 4$–4.5 cm travel an average of 1.3 mm toward the center of the lobe for the 800 eV case, but only 0.1 mm for the 100 eV case. Second and more importantly, our simulations showed that most electrons that enter and land in the lobe regions come from secondary electrons generated near the lobe region. As shown in Figure 9, the secondary electron production rates at $R = 1.5$–2.5 cm and $R = 4$–5 cm are much higher in the 800 eV case than in the 100 eV case due to higher ion energies hitting the surface as described above. Therefore, more secondary electrons are able to enter the lobe region in the 800 eV case, causing the surface potential to be lower than the beam energy.

These results suggest that a combination of outward pointing surface electric fields and an increased number of ion-induced secondary electrons near the lobe regions for higher energy beams may result in a higher number of electrons moving into the shielded lobe regions, causing reduced positive surface potentials therein. For a more complete understanding, a fully self-consistent study examining these effects would be warranted.

4. Summary and Discussion

The interaction of solar wind with LMAs was studied in a laboratory setup where high-energy flowing plasmas interacted with a magnetic dipole field that engulfed an insulating surface in the CSWE facility. Ion beam energies ranged between 100 and 800 eV. It was found that the surface in the cusp region was charged to a slightly negative potential by the electrons. Highly positive potentials were measured at the surface in the dipole lobe
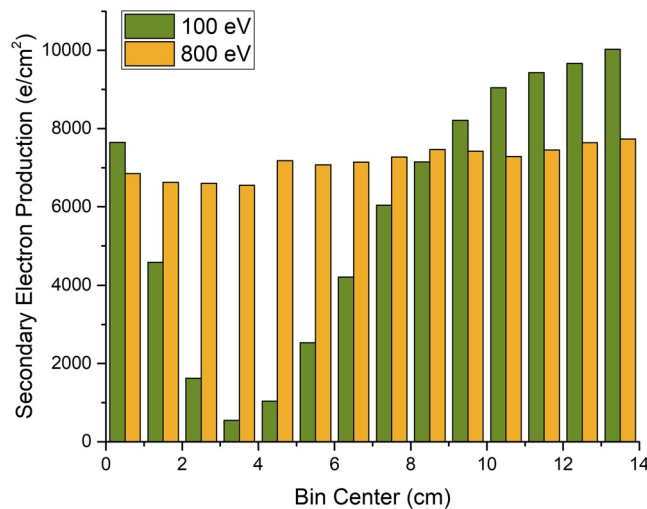
Figure 9. Secondary electron density as a function of radius from the center of the plate when 48,000 electrons are launched in accordance with production rates determined from Knudsen and Harris (1973) and Whipple (1981).
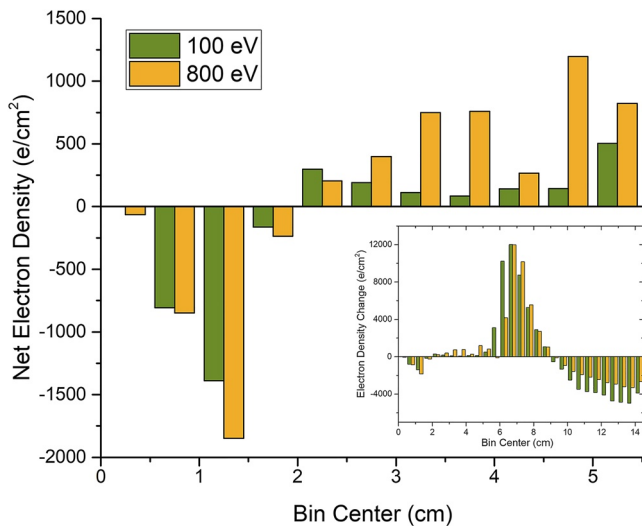
Figure 10. Net density of electrons emitted and collected on the surface as a function of radius from the center of the plate. Inset shows a larger spatial range. Positive net density indicates more collected electrons than emitted electrons and vice versa.

regions, where the incoming electrons were shielded by the magnetic field and the un-magnetized beam ions were able to reach the surface. This positive surface potential followed the beam energy (in eV) up till 200 eV but remained significantly below the beam energy when it was higher than 200 eV. At lower ion beam energies, our results agree with theoretical expectations and findings from previous studies — a surface in an electron-shielded region is charged to a potential that equals the beam energy of incoming singly charged ions (divided by the elementary charge) to stop them, resulting in a zero net current to the surface.

Under higher energy plasma flows, electrons were detected in the shielded lobe regions. Several investigations were performed in order to identify the mechanisms causing the presence of electrons in these regions. Results from a test particle simulation indicated that secondary electrons are produced at the surface due to high-energy ion impacts, and are then transported into the shielded lobe regions via surface electric fields, lowering the surface potential. As magnetic field configurations in LMA regions on the Moon are more complex than a simple dipole used in the laboratory study, the structures of the electric fields in these regions on the lunar surface are expected to be more elaborate than shown in our experiment.

Our study indicates that the lunar surface in some smaller scale LMA regions may charge to large positive potentials but are limited by photoelectrons or secondary electrons emitted from the surface being transported into the electron-shielded regions. Secondary electron production is expected to increase as the ion beam energy approaches typical solar wind ion energies of more than 1 keV (Whipple, 1981). However, the secondary emission yield depends on several factors, such as ion species, surface composition and roughness etc. In-situ measurements of surface potentials and plasma fluxes in LMAs are needed to determine the true effect of ion-induced secondary electrons on the surface charging in these regions. Strong electric fields and secondary electron production mean that space weathering effects and charged dust dynamics in these LMA regions can be different from those in large scale LMA regions and non-LMA regions.

Data Availability Statement

The experimental and simulation data for this paper are available in Zenodo, doi:10.5281/zenodo.5771137.

References

Blewett, D. T., Coman, E. I., Hawke, B. R., Gillis-Davis, J. J., Purucker, M. E., & Hughes, C. G. (2011). Lunar swirls: Examining crustal magnetic anomalies and space weathering trends. *Journal of Geophysical Research*, *116*(E2). https://doi.org/10.1029/2010JE003656

Böhm, C., & Perrin, J. (1993). Retarding-field analyzer for measurements of ion energy distributions and secondary electron emission coefficients in low-pressure radio frequency discharges. *Review of Scientific Instruments*, *64*(1), 31–44. https://doi.org/10.1063/1.1144398

Deca, J., Divin, A., Lapenta, G., Lembege, B., Markidis, S., & Horanyi, M. (2014). Electromagnetic particle-in-cell simulations of the solar wind interaction with lunar magnetic anomalies. *Physical Review Letters*, *112*, 151102. https://doi.org/10.1103/physrevlett.112.151102

Deca, J., Divin, A., Lembège, B., Horányi, M., Markidis, S., & Lapenta, G. (2015). General mechanism and dynamics of the solar wind interaction with lunar magnetic anomalies from 3-d pic simulations. *Journal of Geophysical Research: Space Physics*, *120*, 6443–6463. https://doi.org/10.1002/2015JA021070

Deca, J., Divin, A., Lue, C., Ahmadi, T., & Horányi, M. (2018). Reiner gamma albedo features reproduced by modeling solar wind standoff. *Nature Communications Physics*, *1*(12). https://doi.org/10.1038/s42005-018-0012-9

Diebold, D., Hershkowitz, N., Bailey, A. D., Cho, M. H., & Intrator, T. (1988). Emissive probe current bias method of measuring dc vacuum potential. *Review of Scientific Instruments*, *59*(2), 270–275. https://doi.org/10.1063/1.1140239

Fatemi, S., Lue, C., Holmström, M., Poppe, A. R., Wieser, M., Barabash, S., & Delory, G. T. (2015). Solar wind plasma interaction with gerasimovich lunar magnetic anomaly. *Journal of Geophysical Research*, *120*, 4719–4735. https://doi.org/10.1002/2015JA021027

Futaana, Y., Barabash, S., Wieser, M., Lue, C., Wurz, P., Vorburger, A., et al. (2013). Remote energetic neutral atom imaging of electric potential over a lunar magnetic anomaly. *Geophysical Research Letters*, *40*, 262–266. https://doi.org/10.1002/grl.50135

Garrick-Bethell, I., Head, J. W., III, & Pieters, C. M. (2011). Spectral properties, magnetic fields, and dust transport at lunar swirls. *Icarus*, *212*(2), 480–492. https://doi.org/10.1016/j.icarus.2010.11.036

Gibson, J., & Coppins, M. (2018). Theory of electron density in a collisionless plasma in the vicinity of a magnetic dipole. *Physics of Plasmas*, *25*(11), 112103. https://doi.org/10.1063/1.5053486

Glotch, T. D., Bandfield, J. L., Lucey, P. G., Hayne, P. O., Greenhagen, B. T., Arnold, J. A., et al. (2015). Formation of lunar swirls by magnetic field standoff of the solar wind. *Nature Communications*, *6*, 6189. https://doi.org/10.1038/ncomms7189

Halekas, J. S., Brain, D. A., Mitchell, D. L., Lin, R. P., & Harrison, L. (2006). On the occurrence of magnetic enhancements caused by solar wind interaction with lunar crustal fields. *Geophysical Research Letters*, *33*(8). https://doi.org/10.1029/2006GL025931

Halekas, J. S., Delory, G. T., Brain, D. A., Mitchell, D. L., & Lin, R. P. (2008). Density cavity observed over a strong lunar crustal magnetic anomaly in the solar wind: A mini-magnetosphere? *Planetary and Space Science*, *56*, 941–946. https://doi.org/10.1016/j.pss.2008.01.008

Harnett, E. M., & Winglee, R. M. (2000). Two-dimensional mhd simulations of the solar wind interaction with magnetic field anomalies on the surface of the moon. *Journal of Geophysical Research*, *105*(24), 24997–25008. https://doi.org/10.1029/2000ja000074

Hashimoto, K., Hashitani, M., Kasahara, Y., Omura, Y., Nishino, M. N., Saito, Y., et al. (2010). Electrostatic solitary waves associated with magnetic anomalies and wake boundary of the Moon observed by KAGUYA. *Geophysical Research Letters*, *37*, L19204. https://doi.org/10.1029/2010GL044529

Hemingway, D. J., Garrick-Bethell, I., & Kreslavsky, M. A. (2015). Latitudinal variation in spectral properties of the lunar maria and implications for space weathering. *Icarus*, *261*, 66–79. https://doi.org/10.1016/j.icarus.2015.08.004

Hendrix, A., Greathouse, T., Retherford, K., Mandt, K., Gladstone, G., Kaufmann, D., et al. (2016). Lunar swirls: Far-uv characteristics. *Icarus*, *273*, 68–74. https://doi.org/10.1016/j.icarus.2016.01.003

Hood, L., & Schubert, G. (1980). Lunar magnetic anomalies and surface optical properties. *Science*, *208*(4439), 49–51. https://doi.org/10.1126/science.208.4439.49

Howes, C., Wang, X., Deca, J., & Horányi, M. (2015). Laboratory investigation of lunar surface electric potentials in magnetic anomaly regions. *Geophysical Research Letters*, *42*(11), 4280–4287. https://doi.org/10.1002/2015gl063943

Jarvinen, R., Alho, M., Kallio, E., Wurz, P., Barabash, S., & Futaana, Y. (2014). On vertical electric fields at lunar magnetic anomalies. *Geophysical Research Letters*, *41*, 2243–2249. https://doi.org/10.1002/2014gl059788

Knudsen, W. C., & Harris, K. K. (1973). Ion-impact-produced secondary electron emission and its effect on space instrumentation. *Journal of Geophysical Research*, *78*(7), 1145–1152. https://doi.org/10.1029/ja078i007p01145

Kramer, G. Y., Besse, S., Dhingra, D., Nettles, J., Klima, R., Garrick-Bethell, I., et al. (2011). M3 spectral analysis of lunar swirls and the link between optical maturation and surface hydroxyl formation at magnetic anomalies. *Journal of Geophysical Research*, *116*(E9). https://doi.org/10.1029/2010je003729

Kramer, G. Y., Combe, J.-P., Harnett, E. M., Hawke, B. R., Noble, S. K., Blewett, D. T., et al. (2011). Characterization of lunar swirls at mare ingenii: A model for space weathering at magnetic anomalies. *Journal of Geophysical Research*, *116*(E4), E04008. https://doi.org/10.1029/2010je003669

Lin, R. P., Mitchell, D. L., Curtis, D. W., Anderson, K. A., Carlson, C. W., McFadden, J., et al. (1998). Lunar surface magnetic fields and their interaction with the solar wind: Results from lunar prospector. *Science*, *281*(5382), 1480–1484. https://doi.org/10.1126/science.281.5382.1480

Lue, C., Futaana, Y., Barabash, S., Wieser, M., & Holmstrom, M. (2011). Strong influence of lunar crustal fields on the solar wind flow. *Geophysical Research Letters*, *38*, L03202. https://doi.org/10.1029/2010gl046215

Mitchell, D. L., Halekas, J. S., Lin, R. P., Frey, S., Hood, L. L., Acuña, M. H., & Binder, A. (2008). Global mapping of lunar crustal magnetic fields by Lunar Prospector. *Icarus*, *194*, 401–409. https://doi.org/10.1016/j.icarus.2007.10.027

Pinet, P. C., Shevchenko, V. V., Chevrel, S. D., Daydou, Y., & Rosemberg, C. (2000). Local and regional lunar regolith characteristics at reiner gamma formation: Optical and spectroscopic properties from clementine and earth-based data. *Journal of Geophysical Research*, *105*(E4), 9457–9475. https://doi.org/10.1029/1999je001086

Russell, C. T., & Lichtenstein, B. R. (1975). On the source of lunar limb compressions. *Journal of Geophysical Research*, *80*(34), 4700–4711. https://doi.org/10.1029/JA080i034p04700

Saito, Y., Nishino, M. N., Fujimoto, M., Yamamoto, T., Yokota, S., Tsunakawa, H., et al. (2012). Simultaneous observation of the electron acceleration and ion deceleration over lunar magnetic anomalies. *Earth Planets and Space*, *64*(2), 4. https://doi.org/10.5047/eps.2011.07.011

Saito, Y., Yokota, S., Asamura, K., Tanaka, T., Nishino, M. N., Yamamoto, T., et al. (2010). In-flight performance and initial results of plasma energy angle and composition experiment (pace) on selene (kaguya). *Space Science Reviews*, *154*(1), 265–303. https://doi.org/10.1007/s11214-010-9647-x

Schultz, P. H., & Srnka, L. J. (1980). Cometary collisions on the moon and Mercury. *Nature*, *284*, 22–26. https://doi.org/10.1038/284022a0

Smith, J. R., Hershkowitz, N., & Coakley, P. (1979). Inflection-point method of interpreting emissive probe characteristics. *Review of Scientific Instruments*, *50*(2), 210–218. https://doi.org/10.1063/1.1135789

Starukhina, L. V., & Shkuratov, Y. G. (2004). Swirls on the moon and mercury: Meteoroid swarm encounters as a formation mechanism. *Icarus*, *167*(1), 136–147. https://doi.org/10.1016/j.icarus.2003.08.022

Ulibarri, Z., Han, J., Horányi, M., Munsat, T., Wang, X., Whittall-Scherfee, G., & Yeo, L. H. (2017). A large ion beam device for laboratory solar wind studies. *Review of Scientific Instruments*, *88*(11), 115112. https://doi.org/10.1063/1.5011785

Usui, H., Miyake, Y., Nishino, M. N., Matsubara, T., & Wang, J. (2017). Electron dynamics in the minimagnetosphere above a lunar magnetic anomaly. *Journal of Geophysical Research*, *122*, 1555–1571. https://doi.org/10.1002/2016JA022927

Wang, H. Z., Xiao, C., Shi, Q. Q., Guo, R. L., Yue, C., Xie, L. H., et al. (2021). Energetic neutral atom distribution on the lunar surface and its relationship with solar wind conditions. *The Astrophysical Journal Letters*, *922*(2), L41. https://doi.org/10.3847/2041-8213/ac34f3

Wang, X., Horányi, M., & Robertson, S. (2012). Characteristics of a plasma sheath in a magnetic dipole field: Implications to the solar wind interaction with the lunar magnetic anomalies. *Journal of Geophysical Research*, *117*(A6), A06226. https://doi.org/10.1029/2012JA017635

Wang, X., Howes, C., Horányi, M., & Robertson, S. (2013). Electric potentials in magnetic dipole fields normal and oblique to a surface in plasma: Understanding the solar wind interaction with lunar magnetic anomalies. *Geophysical Research Letters*, *40*(9), 1686–1690. https://doi.org/10.1002/grl.50367

Whipple, E. C. (1981). Potentials of surfaces in space. *Reports on Progress in Physics*, *44*(11), 1197. https://doi.org/10.1088/0034-4885/44/11/002

Wieser, M., Barabash, S., Futaana, Y., Holmstrom, M., Bhardwaj, A., Sridharan, R., et al. (2010). First observation of a mini-magnetosphere above a lunar magnetic anomaly using energetic neutral atoms. *Geophysical Research Letters*, *37*, L015103. https://doi.org/10.1029/2009gl041721

Xie, L., Li, L., Zhang, A., Zhang, Y., Cao, J., Wieser, M., et al. (2021). Inside a lunar mini-magnetosphere: First energetic neutral atom measurements on the lunar surface. *Geophysical Research Letters*, *48*(14), 3937–3945. https://doi.org/10.1029/2021GL093943

Zimmerman, M. I., Farrell, W. M., & Poppe, A. R. (2015). Kinetic simulations of kilometer-scale minimagnetosphere formation on the moon. *Journal of Geophysical Research: Planets*, *120*(11), 1893–1903. https://doi.org/10.1002/2015JE004865